Evaluation of spalling of concrete pieces from tunnel lining employing joint shear model

Kiwamu Tsuno[1]*, Kiyoshi Kishida[2]

[1] *Railway Technical Research Institute, Kokubunji, Tokyo, 185-8540, Japan*

E-mail address: tsuno.kiwamu.00@rtri.or.jp

[2] *Department of Urban Management, Kyoto University, Kyoto, 615-8540, Japan*

* Corresponding author.

E-mail address: tsuno.kiwamu.00@rtri.or.jp (K. Tsuno)

ABSTRACT

This paper was conducted to quantify the spalling of tunnel lining concrete. This paper firstly modeled the spalling of tunnel lining concrete and examined ways to quantitatively evaluate the safety of the tunnel lining concrete against spalling by comparing the shear stress acting on the joint surfaces of lining concrete cracks with the shear capacity of the joint surfaces. Secondly, based on double shear tests simulating the spalling phenomenon, it was found that wider crack widths as well as greater tapered angles of the joint surfaces resulted in lower shear capacities. Thirdly, a method for simulating the shearing process of joint surfaces was proposed. The method was shown to be able to roughly estimate the relationship between the joint aperture and the shear capacity. Using the improved method, the shear capacity was considered using various widths and tapered angles of the cracks. Furthermore, it was found that the *JRC* value of the joint surface samples collected from actual tunnels was between the *JRC* value of the mortar beam joint surfaces that were made in the shear test and that of the joint surfaces of the concrete beam, made in the shear tests with the maximum aggregate size measuring 40 mm. A parameter study was also conducted under hypothetical conditions for the relationship between the width of the cracks and the safety of the tunnel lining against spalling.

Keywords:

Tunnel lining

Falling of concrete fragments

Shear strength

Crack surface roughness

1. INTRODUCTION

The problem of the spalling of tunnel lining concrete started drawing attention after the spalling accident involving a Shinkansen (bullet train) railway tunnel in 1999 in Japan, as shown in Figures 1 and 2 (Ministry of Transport, 2000; Asakura et al., 2001). Railway and road tunnels are periodically examined through visual inspections and hammering tests to evaluate their structural soundness. When areas at risk of spalling are found, appropriate actions are taken to ensure the safety of the tunnel. In the maintenance of railway tunnels, visual inspections are firstly conducted which may reveal multiple connected cracks in closed, crossed, parallel or other forms. These are followed by hammering tests, in which the tunnel linings are hit with a hammer or similar object. Based on the results, the tunnel's structural soundness against spalling is rated as α, β or γ. For example, if an area with closed cracks emits a dull sound when hit, the area's structural soundness is rated as α, in which case measures to prevent spalling must be taken.

In an ordinary inspection, the tunnel lining surfaces are visually inspected for cracks, including their shapes and widths. Cracks seen on tunnel lining surfaces have a range in widths, from small to large, and it is assumed that closed cracks with greater widths have a greater risk of spalling. The current method used for evaluating structural soundness is based on a qualitative approach in which the risk of spalling is considered to be greater with multiple closed cracks. No methods for quantitatively evaluating the safety against spalling have been proposed; and thus, there are no criteria available today on the specific widths of cracks for a quantitative evaluation of the structural soundness. If there were a method of quantitatively evaluating the relationship between the widths of lining surface cracks and the safety against spalling, the structural soundness against spalling could be determined more accurately, which would contribute to the rational maintenance of tunnels.

In mountain tunnels with plain concrete linings, for which there is no adhesion of the concrete to reinforcing bars, any closed cracks that run across the width of the lining can cause spalling. In practice, the risk of closed cracks causing concrete to spall off is reduced by the roughness of the mating faces of the cracks causing frictional resistance. Therefore, the safety of the tunnel lining against spalling is thought to vary widely depending on the roughness and the width of the cracks.

Some studies have investigated the anomalies of tunnel linings caused by outer force, such as squeezing earth pressure, uneven earth pressure, loosening earth pressure, etc. For example, Asakura et al. (1994) carried out loading tests with 1/30 scaled lining models and arranged the relationship between the loading patterns and the configurations of the cracks observed in the tunnel lining. He et al. (2009) investigated the failure mechanism of deformed tunnels. Wang (2010) and Chiu et al. (2017) investigated the anomalies of tunnel linings caused by the instability of neighboring slopes. However, these studies did not focus on the spalling of the tunnel lining, which is a local phenomenon.

With reinforced concrete, a number of studies have examined the shear capacity and the stress transfer that factor into the roughness of concrete cracks and joints (Yoshikawa and Tanabe, 1986; Yoshikawa et al., 1989; Li and Maekawa, 1988; Maekawa and Qureshi, 1997). Chiaia et al. (2009) also investigated the effect of fibers in the tunnel lining concrete by means of a block model. However, there have been few studies on the spalling of pieces of plain concrete attributable to the concrete's own weight, wind pressure, and other factors. The following is an example of studies conducted on the plain concrete linings of road tunnels: a study in which cracking modes were examined for factors involved in spalling and a study in which core samples of cracked linings were collected and their shear strength was measured by direct shear tests (Ito et al., 2004). Those studies provided valuable data for investigating the spalling of tunnel lining concrete, but did not propose quantitative methods for evaluating spalling, including the relationship between the width of a crack, as well as the degree of roughness of the mating faces of the crack (hereinafter defined as joint surface roughness), and the safety against spalling.

With this background, the authors firstly modeled the spalling of tunnel lining concrete and examined ways to quantitatively evaluate the safety against the spalling of the tunnel lining concrete by comparing the shear stress acting on the joint surfaces of lining concrete cracks with the shear capacity of the joint surfaces. Secondly, double shear tests simulating the spalling phenomenon were conducted to clarify the relationship between the width and tapered angle of the cracks and the shear capacity. Thirdly, double shear tests were simulated using an improved method to replicate direct shear tests on rock joints (Kishida and Tsuno, 2001), and its applicability was examined. Employing the method, the shear capacity was considered using various widths and tapered angles of the cracks and various material strengths. Furthermore, the joint surface roughness in an actual tunnel was measured, and calculations were performed under hypothetical conditions for the relationship between the width of the cracks and the safety of the tunnel lining against spalling.

2. MODELING THE SPALLING OF TUNNEL LINING CONCRETE

2.1 Modeling of the spalling

In the past, pieces of concrete that fell off the lining of mountain tunnels were typically several centimeters thick; and thus, the events were categorized as exfoliation. During one such accident, however, a chunk of concrete (250 cm wide, 300 cm deep, and 45 cm thick) fell off the crown of a railway tunnel, as shown in Figure 2. Such huge chunks of concrete could cause serious accidents. Therefore, the present study looked at the spalling of huge chunks of lining concrete. While spalling can also be caused by other factors, such as a void behind the lining, the aim of this study is to model the spalling phenomenon that is caused by a reduced shear capacity of the joint surfaces of cracks that have become wider apart or are due to other characteristics.

The falling of a chunk of plain lining concrete from the crown of a mountain tunnel was modeled as follows: It was assumed that the concrete piece was formed by the closure of cracks and had the dimensions of B by D by H shown in Figure 3.

1) The weight of the chunk and the external forces generate shear stress τ_a that acts on the joint surfaces (the four sides of the chunk) of the cracks.

2) Shear resistance is generated as a result of the roughness of the joint surfaces of the cracks. The maximum shear resistance, which depends on the joint surface roughness, the strength of the chunk material, and other factors, is defined as the shear capacity τ_b of the joint surfaces.

3) The chunk falls off when shear stress τ_a, acting on the joint surfaces, exceeds the shear capacity τ_b of the joint surfaces.

While possible adhesion to the ground and to waterproof sheets behind the lining can have an influence on the shear capacity, those factors were not considered in the model. This is because it is difficult to assess such adhesion appropriately and because the model used in the evaluation was on the safe side.

2.2 Shear stress generated on the joint surfaces of cracks

In the case of Figure 3, shear stress τ_{a1} generated by the weight of the chunk can be calculated as follows:

$$W = \gamma BDH \tag{1}$$

$$A = 2H(B + D) \tag{2}$$

$$\tau_{a1} = \frac{W}{A} = \frac{\gamma BD}{2(B + D)} \tag{3}$$

where:

W: weight of the chunk

γ: weight per unit volume of the chunk

B: width of the chunk

D: depth of the chunk

H: thickness of the chunk

A: area of the joint surfaces of the cracks

Shear stress τ_{a2}, generated by external forces, can be calculated as follows:

$$\tau_{a2} = \frac{fBD}{2H(B+D)} \qquad (4)$$

where:

f: stress caused by external forces (i.e., stress acting on the area measuring B by D)

Based on the above, shear stress τ_a, generated on the joint surfaces of the cracks, can be calculated by

$$\tau_a = \frac{\gamma BD}{2(B+D)} + \frac{fBD}{2H(B+D)} \qquad (5)$$

2.3 Trial calculation of the shear stress generated on the joint surfaces of cracks

The shear stress acting on the joint surfaces of the chunk was calculated under various areas of closed cracks and thicknesses of the chunk using Equation (5). The trial calculation was performed under the same width B and depth D. Only the specific wind pressure of 5 kN/m^2, generated by the passage of trains, was considered as the stress caused by external forces f. For this wind pressure, the variation in air pressure (5 kN/m^2), measured on the Sanyo Shinkansen line during a train passage, was used (Ministry of Transport, 2000).

Figure 4 shows the relationship between the area of closed cracks and the shear stress generated on the joint surfaces of the cracks. The area of closed cracks was calculated by multiplying the width of chunk B by depth D. As the figure shows, for the same thickness of the chunk, larger shear stress is generated on the joint surfaces when the area of the closed cracks is larger. Moreover, for the same area of closed cracks, the shear stress becomes smaller when the chunk is thicker.

3. DOUBLE SHEAR TESTS

3.1 Outline of the tests

To quantitatively evaluate the safety of the tunnel lining concrete against spalling, it is necessary to clarify the shear capacity of the joint surfaces of the cracks relative to the behavior of the area within the closed cracks. Accordingly, mortar test pieces were made, each with two cracks, as shown in

Figure 5, which were then subjected to the double shear tests using the loading device shown in Figure 6 to simulate the falling of a piece of tunnel lining concrete.

3.1.1 Test pieces

The joint surfaces of each crack in the test pieces were made by making a plain concrete beam (2000 mm long, 250 mm wide, and 500 mm high) with the maximum aggregate size measuring 20 mm, and then subjecting the beam to a shear test to generate the crack. In the next step, to ensure uniform roughness on all test pieces, plaster casts of the crack were made and then mortar faces of the crack were created from the plaster casts. Then, the mortar casts were placed in a mold in such a way that, for both cracks of each test piece, the protruding mortar cast with a cracked face (250 × 250 mm) was on the underload section and the receding mortar cast with an identical cracked face was on the stub side. Finally, mortar was poured into the mold and left to cure at air temperature for 28 days. The result was a test piece consisting of left and right stubs with an underload section between them, with the three sections split by two cracks. Using the same procedure, plaster and mortar joints were made to compare their roughness. Only a small difference was found between them that corresponded to a *JRC* value, a measure of the joint surface roughness, of around 0.3 at most.

The test pieces were produced, including the curing process, at a constant room temperature of 20°C. The mortar was made from cement, sand, and water in a weight ratio of 1:2.8:0.6. The tests showed that the mortar had a uniaxial compressive strength of 36 N/mm^2 and a modulus of static elasticity of 2.50×10^4 N/mm^2.

3.1.2 Measurement of the roughness of the joint surfaces

Prior to testing, the roughness of the joint surfaces was measured at intervals of 1 mm using a surface roughness measurement system consisting of a CCD laser displacement meter (spot diameter: 70 μm and resolution: 3 μm) and a sliding table. The measured joint roughness is shown in Figure 7.

The measurements have a *JRC* of 29.0, which roughly agrees with the average of 28.1 for actual tunnels described in 5.1. One specific joint roughness was used, focusing mainly on the effect of the crack width in the tests, although the joint surface roughness is different in actual situations. The effects of the joint surface are discussed in Chapters 5 and 6.

3.1.3 Test cases

The test cases are shown in Table 1. In Cases 1 to 5, the tests were conducted using various crack widths to clarify the relationship between the joint aperture and the shear capacity. In Cases 6 and 7, the joints were tapered to facilitate the falling of the underload section. As described earlier, the joint surfaces in those cases were a copy of the joint surface made in the shear test on a plain concrete beam with the maximum aggregate size measuring 20 mm. Therefore, the joint surfaces all had the same roughness profile.

3.1.4 Test device and method

As shown in Figure 6, the test device consisted primarily of reaction frames, a hydraulic jack to apply vertical load (3,000 kN), and two screw jacks to hold the stub sections still. After a test piece was placed on the test device, the stub sections were held in place with screw jacks to prevent their vertical movement, thereby preventing them from rotating during the test. To allow the stub sections to move horizontally, Teflon plates were inserted between the stub sections and the screw jacks and beneath the stub sections. Having made these arrangements, the underload section was then subjected to a vertical load using a hydraulic jack in a controlled displacement mode (0.015 mm/s).

For the measurements, a load cell was placed between the hydraulic jack and the underload section to measure the shear stress, while load cells were placed between the reaction frames and the test pieces to measure the horizontal reaction stress on both sides. In addition, the vertical displacement of the underload section was measured with four displacement sensors (Ch1 to Ch4 in Figure 6 (b)) to obtain the shear displacement, while the horizontal displacements of the stub and the underload sections were measured with 6 displacement sensors (Ch5 to Ch10 in Figure 6 (b)) to obtain the aperture growth of the joint surfaces.

3.2 Test results

3.2.1 Test results of test pieces with various crack widths

Figure 8 (a) shows the relationship between the shear displacement and the shear stress for Cases 1 to 5 with various crack widths. In the tests, as the two joint surfaces contribute to shearing, the shear stress is calculated by dividing the vertical load applied on the underload section by the hydraulic jack by the combined area (2 × 250 × 250 mm) of the two joint surfaces. The figure shows that the shear stress grew as the shear displacement increased until a certain point at which the test pieces yielded and the maximum shear stress was reached. Beyond that point, the shear stress remained approximately the same. It was also found that test pieces with wider crack widths had smaller values of maximum shear stress.

Figure 8 (b) shows the relationship between the shear displacement and the horizontal reaction stress. The horizontal reaction stress was obtained by dividing the average stress measured with the load cells (500 kN) on both sides by the combined area of the joint surfaces. The relationship between the shear displacement and the horizontal reaction stress shows similarities to that between the shear displacement and the shear stress. Test pieces with wider crack widths had smaller values of maximum horizontal reaction stress. Likewise, test pieces with wider crack widths had smaller values of aperture growth (Figure 8 (c)). The joint aperture growth of a test piece here is the average value based on the piece’s two joint apertures, starting at 0 mm when the shear displacement is 0 mm.

3.2.2 Test results of test pieces with various tapered angles of joint surfaces

Figure 9 shows the relationship between the shear displacement and the shear stress for Cases 1, 6, and 7 with different tapered angles of the joint surfaces. As shown in the figure, with the tapered angles of 5° and 10°, the shear stress rose as the shear displacement increased. Then, after peaking, it declined. It was also found that the test pieces with greater tapered angles of the joint surfaces had smaller values of maximum shear stress.

3.2.3 Summary of the test results

The double shear tests, simulating the spalling phenomenon, yielded the following results:

1) The shear stress grew as the shear displacement increased until a certain point at which the maximum shear stress was reached. Beyond that point, the load approximately remained stable or declined.
2) Test pieces with wider crack widths had smaller values of maximum shear stress, possibly allowing them to fall more easily with weaker external force.
3) Test pieces with greater tapered angles of the joint surfaces had smaller values of maximum shear stress, possibly allowing them to fall more easily with weaker external force.

4. SIMULATION OF THE SPALLING OF TUNNEL LINING CONCRETE

4.1 Outline of the analysis

In the double shear tests described in the previous section, test pieces were examined that all had the same roughness of joint surfaces and were made of the same material. However, the shear capacity is thought to change with the roughness and the material properties. Accordingly, methods for simulating the shearing process of joints were examined to clarify the shear capacity for varying roughness and material properties of joints.

In rock engineering, equations and models for the shearing behavior of rock joints have been developed (Patton, 1966; Barton, 1973; Barton and Choubey, 1977; Ohnishi et al., 2000; Kishida and Tsuno, 2001). Among them, the examination in this study was based on an analytical model (Kishida and Tsuno, 2001) that is designed to simulate the post-peak shearing behavior of rock joints, from softening up to the residual state, based on the inputs of confining pressure, material strength, material friction angle, and three-dimensional digitized joint surface roughness data. The analytical model used in this study was based on the following:

1) In the shearing process, confining pressure acts on the asperities (surface unevenness between the measuring points) in contact with each other where stress concentrates.

2) As the area of contact depends on the angle of dilation (between the direction in which the test piece moves in shearing and dilation and the shearing direction) and the profile of the roughness, the stress concentrated on the asperities in contact with each other can be determined based on an assumed dilation angle.

3) The angle of dilation is determined in such a way that the concentrated stress acting perpendicularly on the asperities in contact with each other at the joint surfaces equals the uniaxial compressive strength.

Although the crack width might be gradually varied along the thickness direction, the proposed method assumes that the crack with is uniform in the thickness direction. It is well known that the joint surface roughness of a rock fracture changes under the shearing process. In addition, the condition of the joint surface roughness, such as the asperities and the contact conditions, strongly affects the mechanical and hydro-mechanical behavior of the rock fracture. Kishida, et al. (2009) carried out direct shear and flow through experiments on single rock joints in additional to flow simulations using joint surface roughness data from the shear analytical model (Kishida and Tsuno, 2001). Obtaining a good agreement between the results of the flow through experiments and the flow simulation of the single rock fractures, the validity of the shear analytical model is confirmed. In this study, the shear analytical model (Kishida and Tsuno, 2001), designed for direct shear tests on joints that are initially engaged completely under constant confining pressure, was modified for the analysis in this study so that it would be able to address the constant stiffness condition and the joint aperture that were considered in the double shear tests.

4.1.1 Analysis steps

The step intervals of the analytical model need to be integer multiples of the measuring intervals of roughness. As the joint surface roughness was measured at 1-mm intervals in the double shear tests, the shear displacement was seen to increase by 1 mm at each step of the analysis. The surface unevenness between two adjoining measuring points was defined as an asperity. In addition, the analysis assumed that the underload section of a test piece would move downward under shearing force. While the joint surfaces had an identical profile in the double shear tests, the simulation considered horizontal reaction stress σ_n and shear stress τ acting on just one of the identical surfaces.

4.1.2 Calculations in Step *i*

With the selected asperities shown in Figure 10, that are in contact with each other and have a dilation angle of σ_{ni}', the horizontal reaction stress acting on the asperities can be calculated by

$$\sigma_{ni}' = \sigma_{ni} \times T / A_i \qquad (6)$$

where:

σ_{ni}: horizontal reaction stress in Step i

T: total number of surfaces between two adjoining measuring points (total number of asperities)

A_i: number of asperities in contact with each other in Step i

As constant stiffness is considered, horizontal reaction stress σ_{ni} was calculated by

$$\sigma_{ni} = K \times \left(1.0 \times \sum_{k=1}^{i-1} \tan\theta_k + 1.0 \times \tan\theta_i \right) \qquad (7)$$

where:

K: spring constant

θ_k: dilation angle determined in Step k

θ_i: assumed dilation angle

Next, horizontal reaction stress σ_{ni}' and shear stress τ_i', acting on the asperities in contact with each other, can be resolved into stress P perpendicular to the joint surface and stress Q parallel to the surface, as shown in Figure 10. With the length of the joint surface given by 1/cos θ, P and Q can be calculated using the following equations:

$$P = (\tau_i' \sin\theta_i + \sigma_{ni}' \cos\theta_i) \times \cos\theta_i \tag{8}$$

$$Q = (\tau_i' \cos\theta_i - \sigma_{ni}' \sin\theta_i) \times \cos\theta_i \tag{9}$$

On the joint surface, the following equation of balance is assumed to be true:

$$Q - P\tan\phi_b = 0 \tag{10}$$

where:

ϕ_b: material friction angle

By substituting Equations (8) and (9) into Equation (10), the following equation is obtained:

$$\tau_i' = \frac{\sigma_{ni}'(\sin\theta_i + \cos\theta_i \tan\phi_b)}{\cos\theta_i - \sin\theta_i \tan\phi_b} \tag{11}$$

Rearranging the equation leads to the following equation, which shows the relationship between σ_{ni}' and τ_i':

$$\tau_i' = \sigma_{ni}' \tan(\phi_b + \theta_i) \tag{12}$$

Furthermore, considering that the ratio of σ_{ni} to σ_{ni}' is equal to the ratio of τ_i to τ_i', the following equation is true:

$$\tau_i = \sigma_{ni} \tan(\phi_b + \theta_i) \quad (13)$$

In Step *i*, the flow chart shown in Figure 11 is followed to determine shear stress τ_i using an assumed dilation angle. Firstly, a dilation angle, θ_i, is assumed and σ_{ni}' is calculated using Equation (6). Secondly, τ_i' is calculated using Equation (12), and then σ_{ni}' and τ_i' are substituted into Equation (8) to calculate stress *P* perpendicular to the joint surface. Then, *P* is compared with the uniaxial compressive strength. If *P* is greater than the uniaxial compressive strength, the dilation angle is reduced by 0.1° ($\theta_i = \theta_i$ - 0.1°). This is repeated, reducing θ_i by 0.1° each time until *P* is equal to or less than the uniaxial compressive strength. The dilation angle θ_i, reached at the end of this process, is then determined as the final dilation angle in this step.

It is assumed that when the joint is completely engaged (Case 1 with a joint aperture of 0 mm), only asperities with a slope angle equal to or greater than the dilation angle are in contact with each other and stress concentrates on those asperities. Accordingly, the slope angle is calculated for all asperities (between the measuring points), as shown in Figure 12, and those asperities whose slope angles are equal to or greater than the dilation angle are counted.

As for the number of asperities in contact with each other when the joint is not completely engaged, the number is obtained by calculating *Weight W* for all asperities (between the measuring points) and totaling the calculations. The *W* between measuring point *k*-1, *j* and measuring point *k*, *j* is calculated as follows:

Under the condition whereby the stub and the underload sections are in contact with each other at measuring point *k*-1, *j*: when the slope angle is greater than dilation angle θ_i, the asperity is considered to be in contact, and therefore, *W* = 1; when the slope angle is less than dilation angle θ_i, the asperity is considered not to be in contact, and therefore, *W* = 0.

When the stub and the underload sections are not in contact with each other at measuring point k-1, j, a straight line is drawn at an angle of θ_i from $Y_i(k\text{-}1, j)$ on the underload section to the stub section, as shown in Figure 13, and the intersection of the line and the stub section is defined as the Transit Contact Point (*TCP*). When *TCP* is located between $X_i(k\text{-}1, j)$ and $X_i(k, j)$, the surface between *TCP* and $X_i(k, j)$ is considered to be in contact and *Weight W* is calculated accordingly by

$$W = L / \Delta x \tag{14}$$

where:

L: distance between the x-coordinate of *TCP* and $x = k$

Δx: measuring interval (1.0)

The x-coordinate of *TCP* can be calculated by

$$x = \frac{X_i(k-1, j) - Y_i(k-1, j)}{\tan\theta - X_i(k, j)/\Delta x + X_i(k-1, j)/\Delta x} \tag{15}$$

When *TCP* is not located between $X_i(k\text{-}1, j)$ and $X_i(k, j)$, $W = 0$.

4.1.3 Roughness at the end of Step *i*

At the end of each step, the underload section is moved 1.0 mm in the shearing direction at the dilation angle determined in Step i. When the stub and the underload sections overlap each other ($X_{i+1}(k, j) > Y_{i+1}(k, j)$), they are assumed to be in contact with each other at the middle point of the overlap (Figure 14).

4.2 Analysis conditions and cases

Using the same joint surface roughness that was used in the double shear tests, a simulation was conducted of shear stress τ and horizontal reaction stress σ_n acting on one of the two joint surfaces as well as of the joint aperture growth. The joint aperture growth corresponds to dilation. In calculating the horizontal reaction stress, spring constant K in Equation (7) was set to 1.5 N/mm^3 based on the relationship obtained in the experiments between the joint aperture growth and the horizontal reaction stress as the spring constant K was affected by the stiffness of concrete, screw jack and other factors. The simulation was conducted up to a shear displacement of 16 mm.

The analysis cases used here are shown in Table 2. Cases 1 to 9 employed various crack widths, including those from 5 mm to 8 mm that were not used in the double shear tests. Cases 10 to 15 were conducted with various tapered angles of the joint surface including 15°, 20°, 25°, and 30° that were not used in the double shear tests. Cases 1 to 15 used a uniaxial compressive strength σ_c of 36 N/mm^2.

4.3 Results of the analysis

4.3.1 Results of the analysis with various crack widths

The results of the analysis for Cases 1 to 5 (crack widths of 0 mm to 4 mm), relative to the results of the experiments, are shown in Figure 15. As the roughness of the two crack surfaces was the same as in the double shear tests, the calculation results under the condition of one crack surface are comparable with the experimental ones. The results of Step 1 (shear displacements of 0 mm to 1 mm) are shown at 0.5 mm on the shear displacement axis, while those of Step 2 (shear displacements of 1 mm to 2 mm) are shown at 1.5 mm on the axis. Similar to the results of the experiment, the shear stress grew as the shear displacement increased until the peak was reached, beyond which the shear stress remained approximately stable. It was also found that smaller values of shear stress resulted from wider crack widths. The calculated shear stress slightly differs from the test results in case of crack width if 0mm. It is considered that the difference is caused by the influence of shaved asperities in the shear procedure. As for the horizontal reaction stress and joint aperture growth, smaller values resulted from wider crack widths as in the case of the experiments.

Figure 16 shows the relationship obtained from the analysis of Cases 1 to 9 between the joint aperture and the shear capacity relative to the results of the experiment. The shear capacity corresponds to the maximum shear stress. The results of the analysis roughly agree with those of the experiment, indicating that the simulation method is capable of roughly estimating the relationship between the joint aperture and the shear capacity. It was also found that wider crack widths resulted in lower shear capacities on the joint surfaces.

4.3.2 Results of analysis with various tapered angles of the joint surface

Figure 17 shows the relationship obtained from the analysis of Cases 1 and 10 to 15 between the tapered angle of the joint surface and its shear capacity relative to the results of the experiment. Although there are three experimental results in the figure, the results of the analysis roughly agree with those of the experiment, indicating that the simulation method is capable of roughly estimating the relationship between the tapered angle of joint surfaces and their shear capacity. It was also found that greater tapered angles resulted in lower shear capacities on the joint surface.

4.3.3 Summary of the analysis results

A simulation conducted using the same joint surface roughness that was used in the double shear tests simulating the spalling phenomenon yielded the following findings:

1) The simulation method is capable of roughly estimating the relationship between the joint aperture and the shear capacity and that between the tapered angle of the joint surfaces and the shear capacity.
2) Wider crack widths resulted in lower shear stress and shear capacity of the joint surface.
3) Greater tapered angles of the joint surface resulted in lower shear capacity of the surface.

5. EXAMINATION OF JOINT SURFACE ROUGHNESS

5.1 Joint surface roughness of actual tunnels

Samples of a cracked plain concrete lining were collected by core boring at railway tunnels (double track, around 30 to 40 years old), as shown in Figure 18, and the roughness of the joint surfaces was measured using the method described in 3 (1) b). In rock engineering, indices such as Z_2 and *JRC* have been proposed for the quantification of the joint surface roughness, while equations have been developed for the relationship between Z_2 (Tse and Cruden, 1979) and the *JRC* (Barton and Choubey, 1977). With the core samples, the roughness of the joint surfaces was measured at 0.5-mm intervals over an area measuring 40 mm by 40 mm. To evaluate the roughness in a simplified manner, Z_2 and then the *JRC* were calculated as follows:

$$Z_2 = \left[\frac{1}{M-1} \sum_{i=1}^{M-1} \left(\frac{y_{i+1} - y_i}{\Delta x} \right)^2 \right]^{1/2} \qquad (16)$$

where:

Δx: measuring interval

y_i: height of i^{th} measuring point

M: number of measuring points on a measuring line

$$JRC = 64.22 Z_2 - 2.31 \qquad (17)$$

Figure 19 shows the *JRC* values of the 16 joint surface samples collected from a number of tunnels and those of two cold joint samples that were also collected.

The *JRC* values of the joint surfaces are distributed over a range of 20 to 36, averaging 28.1. The *JRC* values of the cold joint surfaces were smaller than those of the joint surfaces, indicating that the cold joints had lower shear capacity. Cold joints can have a significant impact on spalling as shown by the incident (Ministry of Transport, 2000). It must be noted that cold joints have different characteristics to those of other joints in a closed form with respect to shearing and spalling.

5.2 Surface roughness made in the shear tests on a concrete beam

The double shear tests used a joint surface that was made from a shear test on a concrete beam with the maximum aggregate size measuring 20 mm. Considering that the maximum aggregate size used in railway tunnels that have been built in recent years normally measures 40 mm, a test piece of concrete with the maximum aggregate size measuring 40 mm was made and then subjected to a shear test to obtain the rough surfaces of the cracks. The surfaces were measured at 0.5-mm intervals. A test piece of mortar was also made by following the same procedure, but using no aggregate, and it was also measured at 0.5-mm intervals.

Table 3 shows the *JRC* values that were calculated using the same method as in a). The table reveals that the *JRC* value of the joint surfaces of actual tunnels is between the *JRC* value of the mortar beam joint surfaces and that of the joint surfaces of the concrete beam with the maximum aggregate size measuring 40 mm. In addition, the *JR*C value of the joint surface used in the double shear tests is close to the average *JRC* value of the joint surfaces sampled from actual tunnels. This confirms the validity of using the joint surface used in the double shear tests as a typical roughness profile of the joint surfaces of actual tunnels.

The shear capacity of the joint surfaces of the concrete and mortar beams that were made in the shear tests was calculated. Figure 20 shows the relationship between the calculated shear capacities and the maximum aggregate size. As part of the calculation, the uniaxial compressive strength was 15, 22, 29 36, 43 and 50 N/mm^2 and the tapered angle of the joint surfaces was 0°. As shown in the figure, the shear capacity increases as the maximum aggregate size, or the joint surface roughness, is greater. The shear capacity also increases as uniaxial compressive strengths is larger.

6. EXAMPLE OF CALCULATION OF THE SAFETY AGAINST SPALLING IN ACTUAL TUNNELS

6.1 Outline of calculation

The safety against spalling of the lining concrete was calculated using an index, which was the shear capacity divided by the shear stress of the joint surfaces. A parameter study was conducted using various width B, depth D, and thickness H of a chunk of concrete. Assuming plain concrete with the maximum aggregate size measuring 20 mm, the shear capacity was calculated using the roughness profile used in the double shear tests. In the investigation (Miura et al., 1959), in which core samples of the lining were collected before it was removed as part of the tunnel reconstruction and the samples were subjected to uniaxial compression tests, the uniaxial compressive strength of the samples ranged from 15 N/mm^2 to 26 N/mm^2, as shown in Table 4. Then, the uniaxial compressive strength was set at 15 and 26 N/mm^2. The angles of the joint surfaces found during the core sampling described in 5.1 were 30° or less. Accordingly, the tapered angle of the joint surfaces was set as to be 0° and 30°. As for the wind pressure induced by the train passage, the variation in air pressure (5 kN/m^2) (Ministry of Transport, 2000) measured on the Sanyo Shinkansen line during a train passage was used.

6.2 Calculation results of the safety against spalling

The calculated safety against spalling relative to joint aperture is shown in Figures 21 when the tapered angle of the joint surfaces is 0°. It was found that wider crack widths and larger width B and depth D of chunk of concrete results in lower safety factors against spalling. The safety against spalling is still above 1 even with a joint aperture of 5 mm. Figure 22 shows the calculated safety against spalling when the tapered angle of the joint surfaces is 30°. The tendency of results corresponds to those in Figure 21. Table 5 shows the safety against spalling obtained by Figure 22 under the various size of chunk and uniaxial compressive strength. The safety against spalling increases as uniaxial compressive strengths is larger. In some cases, the safety against spalling is below 1 with a joint aperture of 3 mm. Accordingly, the results of the calculation show that the safety against spalling is considered high when a joint with an aperture of 3 mm or more closes.

The calculations considered only the chunk’s own weight and the train-induced wind pressure as factors contributing to the falling of the chunk. When ground pressure on the tunnel lining is considered, however, the shear stress on the joint surfaces will increase. This aspect requires further study.

7. CONCLUSION

In order to evaluate the spalling of tunnel lining concrete quantitatively, it has been discussed the mechanism through the actual field investigations and its modeling has been presented. Based on this modeling, then, the double shear tests have been conducted. And, the simulation method, which was applied to clarify the shear behavior of rock joints, has been modified and applied to the spalling of tunnel lining concrete. Nest step, the roughness of the cracks in the actual tunnel lining has been measured and the crack width and safety factor against spalling relations has been estimated using the proposed simulation method. The knowledges form this study are summarized below.

- The spalling of tunnel lining concrete was modeled and an equation to calculate the shear stress on the joint surfaces was proposed. Based on that, a method was proposed for quantitatively evaluating the safety against the spalling of the tunnel lining concrete by comparing the shear stress acting on the joint surfaces with the shear capacity of the surfaces.
- Double shear tests, simulating the spalling phenomenon, found that wider crack widths resulted in lower shear capacities of the joint surfaces. Greater tapered angles of the joint surfaces resulted in lower shear capacities.
- A method for simulating the shearing process of joint surfaces was proposed. The method was shown to be able to roughly estimate the relationship between the joint aperture and the shear capacity and that between the tapered angle of the joint surfaces and the shear capacity. Wider crack widths and greater tapered angles of the joint surfaces resulted in lower shear capacities of the joint surfaces with specific rates of decline.
- The *JRC* value of the joint surface samples collected from actual tunnels was between the *JRC* value of the mortar beam joint surfaces that were made in the shear test and that of the joint surfaces of the concrete beam, made in the shear tests with the maximum aggregate size measuring 40 mm.

・Based on a parameter study, it was found that larger width B and depth D and smaller thickness H of chunk of concrete and wider crack widths result in lower safety factors against spalling. The safety against spalling also increases as uniaxial compressive strengths is larger.

It is planned that a quantitative method will be established in the future to judge soundness α, β, and γ by accumulating more data on joint surface profiles and using the proposed method. A simulation method will also be used to examine the effect of measures in preventing spalling.

References

Asakura, T., Kojima, Y., Ando, T., Sato, Y. and Matsuura, A., 1994. Fundamental study on static deformation behavior of tunnel lining, Journal of the Japan Society of Civil Engineers, No. 493/III-27, pp. 79-88.

Asakura, T., Kojima, Y., Onoda, S., Shiroma, H. and Suzuki, I., 2001. Maintenance of tunnels, Proceedings of the International Symposium on Modern Tunneling Science and Technology (IS-Kyoto 2001), Vol. 2, pp. 1139-1164.

Barton, N., 1973. Review of a new shear strength criterion for rock joints, Engineering Geology, pp. 297-306.

Barton, N. and Choubey, V., 1977. The shear strength of rock joints in theory and particles, Rock Mechanics, Vol. 10, pp. 1-65.

Chiaia, B., Fantilli, A. P. and Vallini, P., 2009. Evaluation of crack width in FRC structures and application to tunnel linings, Materials and Structures, Vol. 42, pp. 339-351.

Chiu, T., Lee, C. and Wang, T., 2017. Lining crack evolution of an operational tunnel influenced by slope instability, Tunnelling and Underground Space Technology, Vol. 65, pp. 167-178.

He, W., Kojima, Y. and Asakura, T., 2009. Failure Mechanism of Deformed Concrete Tunnels Subject to Diagonally Concentrated Loads, Computer-aided civil and infrastructure engineering, Vol. 24, Issue 6, pp. 416-431.

Ito, T., Baba, K., Shiroma, H., Yoshitake, I. and Nakagawa, K., 2004. Experiment on the shear strength of crack surface in tunnel lining concrete, journal of the Japan Society of Civil Engineers, No. 777/VI-65, pp. 15-21.

Kishida, K. and Tsuno, K., 2001. The modeling of the shear behavior of rock joints in consideration of the material friction and the joint surface roughness, Journal of the Japan Society of Civil Engineers, No. 680/III-55, pp. 245-261.

Kishida, K., Mgaya, P., Ogura, K. and Hosoda, T., 2009. Flow on a single rock fracture in the shear process and the validity of the cubic law examined through experimental results and numerical simulations, Soils and Foundations, 49(4), pp. 597-610.

Li, B. and Maekawa, K., 1988. Stress transfer constitutive equation for cracked plane of concrete based on the contact plane density function, Concrete Journal, Vol. 26, No. 1, pp. 123-137.

Maekawa, K. and Qureshi, J., 1997. Stress transfer across interfaces in reinforced concrete due to aggregate interlock and dowel action, J. Materials, Conc. Struct., JSCE, No. 557, pp. 159-172.

Ministry of Transport, 2000. Tunnel Safety Issues Study Committee Report, pp. 1-44.

Miura, I., Saigo, K. and Hayakawa, T., 1959. Test on concrete cores and brick (1st report), Railway Technical Research Report, No. 59-261, pp. 4-12.

Ohnishi, Y., Ohtsu, H., Yano, T., Kato, M. and Takada, Y., 2000. The evaluation of shear strength of rock joints based on the digitized roughness profile, Journal of the Japan Society of Civil Engineers, No. 645/III-50, pp. 255-266.

Patton, F. D., 1966. Multiple models of shear failure in rock, Proc. of 1st Int. Congress on Rock Mechanics, ISRM, Vol. 1, pp. 509-513.

Tse, R. and Cruden, D. M., 1979. Estimating joint roughness coefficients, Int. Rock Mech. Min. Sci. & Geomech. Abstr., Vol. 16, pp. 303-307.

Wang, T., 2010. Characterizing crack patterns on tunnel linings associated with shear deformation induced by instability of neighboring slopes, Engineering Geology, Vol. 115, Issue 1-2, pp. 80-95.

Yoshikawa, H. and Tanabe, T., 1986. An analytical study on the mechanical behavior of a single crack in concrete, Journal of the Japan Society of Civil Engineers, No. 372/V-5, pp. 101-110.

Yoshikawa, H., Wu, Z. and Tanabe, T., 1989. Numerical investigation on the nonlinear behavior of crack surface in concrete, Journal of the Japan Society of Civil Engineers, No. 408/V-11, pp. 71-80.

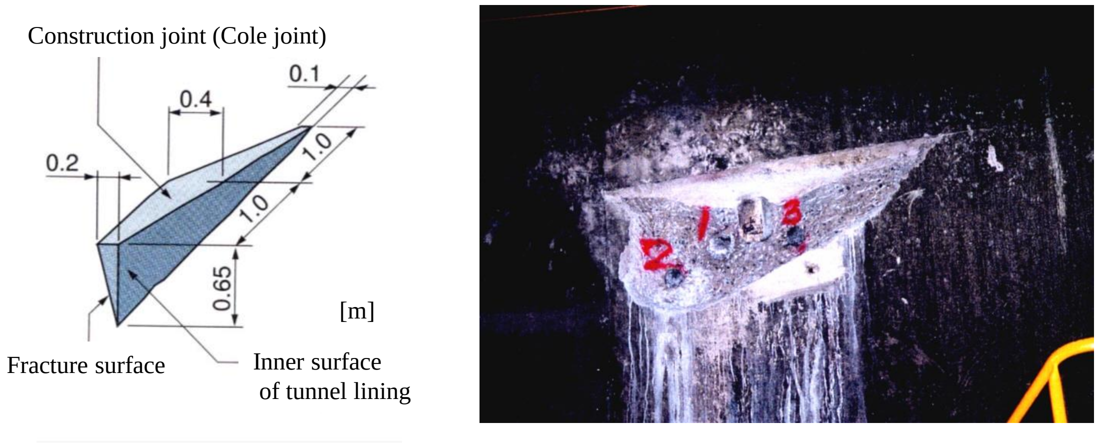

Figure 1 Lining of Fukuoka Tunnel after spalling (Asakura et al., 2001)

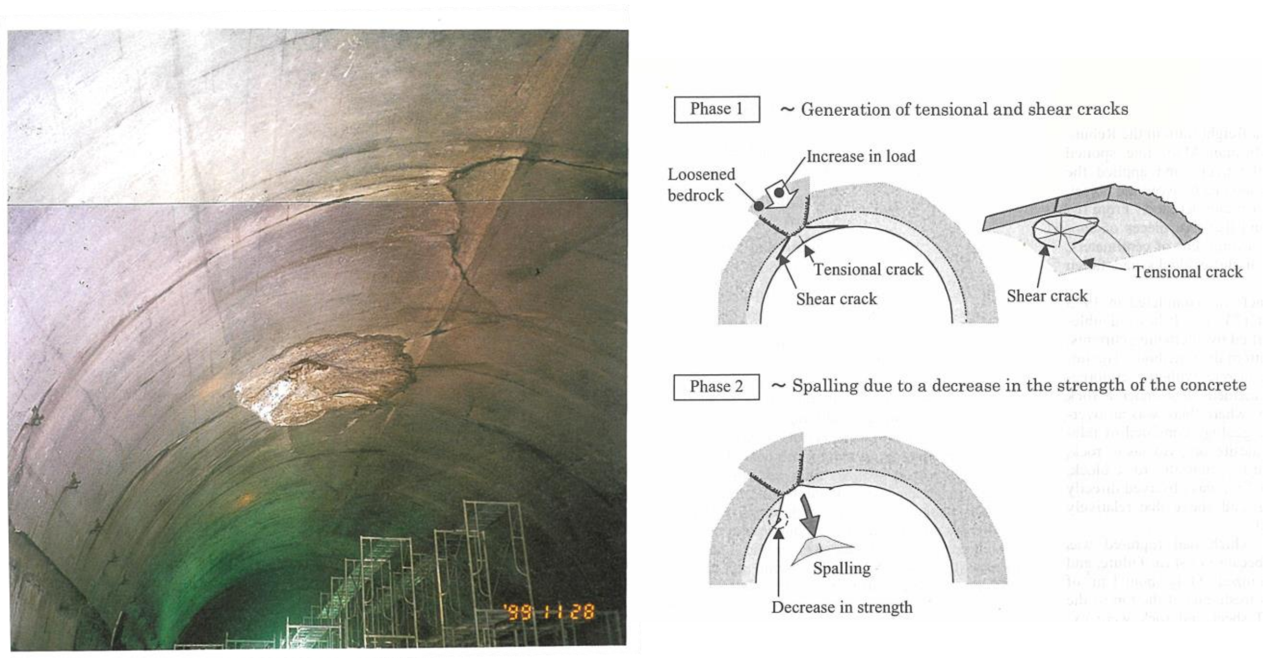

Figure 2 Lining of Rebunhama Tunnel after spalling (Asakura et al., 2001)

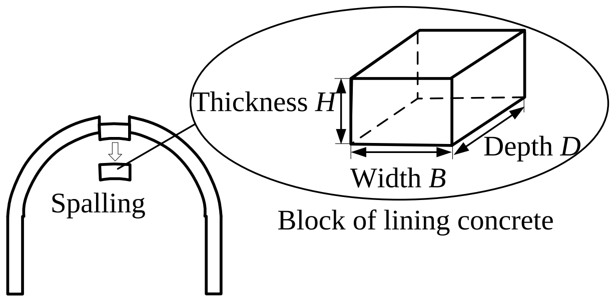

Figure 3 Modeling concepts of spalling

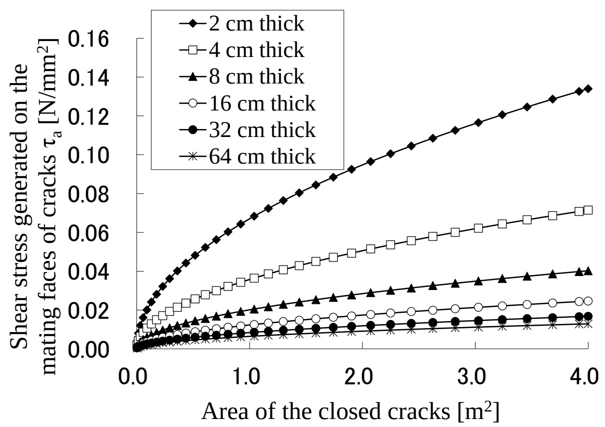

Figure 4 Calculated shear stress generated on the joint surfaces of cracks

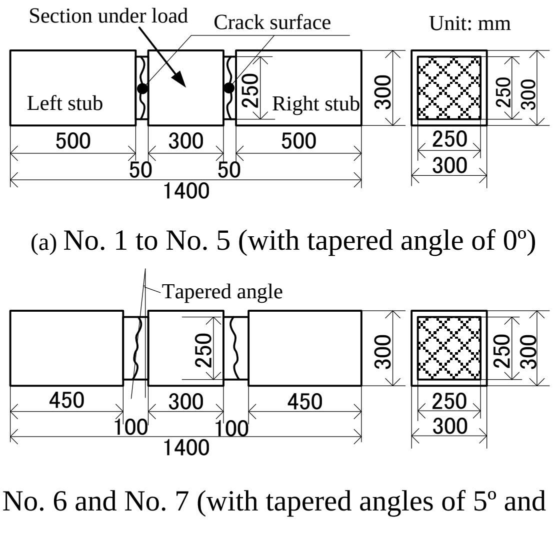

(a) No. 1 to No. 5 (with tapered angle of 0º)

(b) No. 6 and No. 7 (with tapered angles of 5º and 10º)

Figure 5 Test pieces for double shear tests

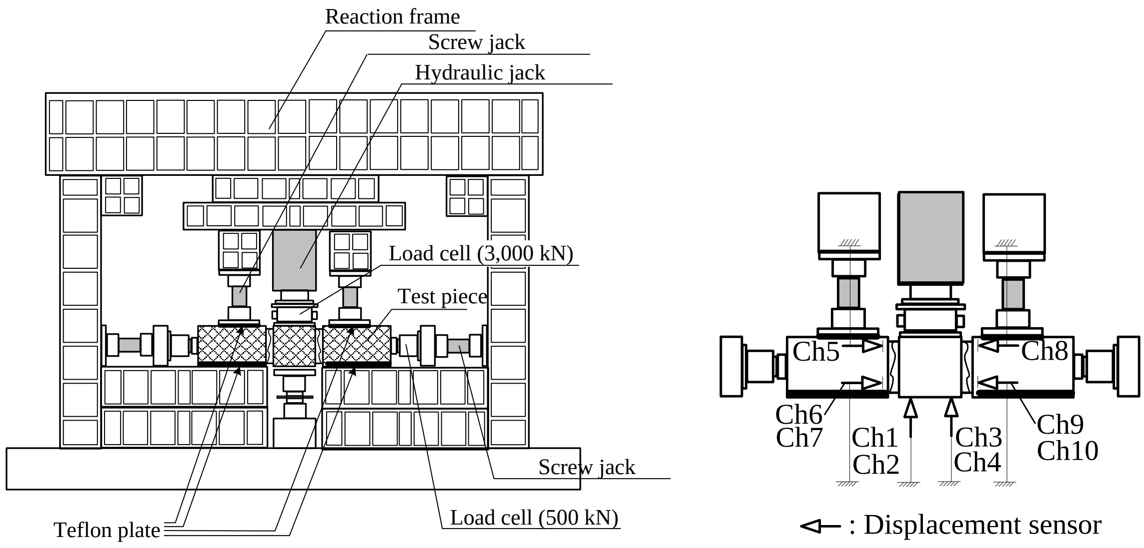

(a) Outline of the loading device

(b) Location of displacement sensor

Figure 6 Outline of the test device

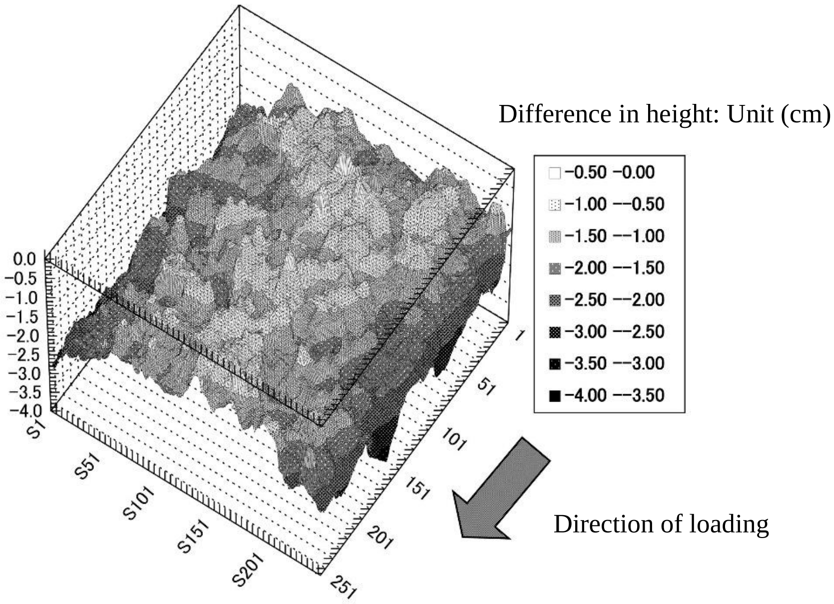

Figure 7 Measured roughness of joint surfaces

Table 1 Test cases

No.	Crack width	Tapered angle of joint surface
1	0 mm	No taper (0°)
2	1 mm	No taper (0°)
3	2 mm	No taper (0°)
4	3 mm	No taper (0°)
5	4 mm	No taper (0°)
6	0 mm	5°
7	0 mm	10°

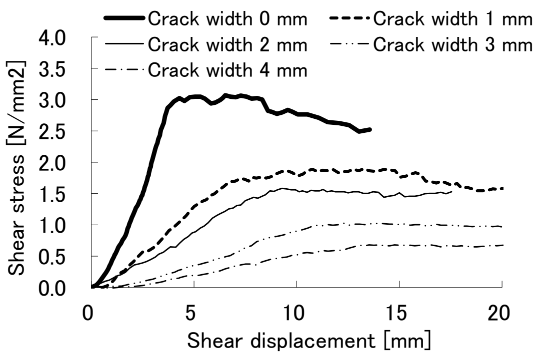

(a) Relationship between shear displacement and shear stress

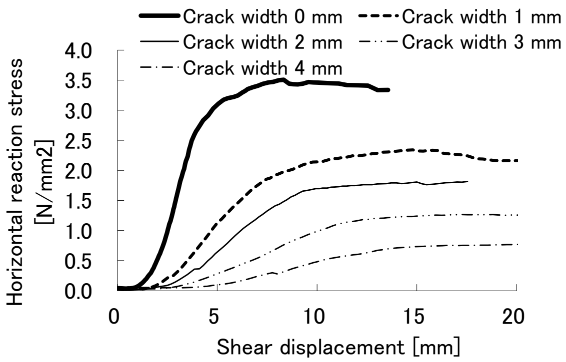

(b) Relationship between shear displacement and horizontal reaction stress

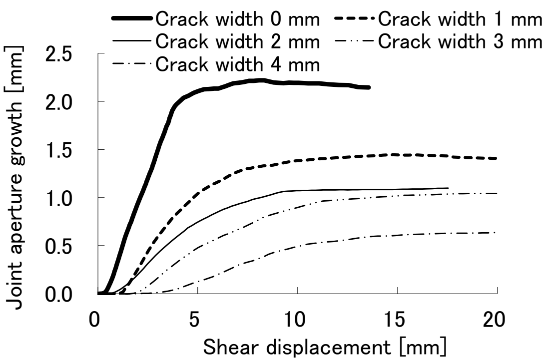

(c) Relationship between shear displacement and joint aperture growth

Figure 8 Test results of test pieces with various crack widths

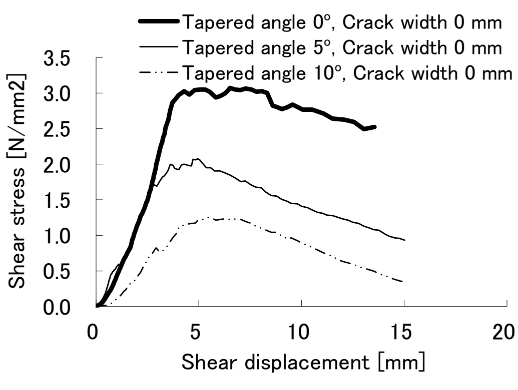

Figure 9 Test results of test pieces with various tapered angles of joint surfaces

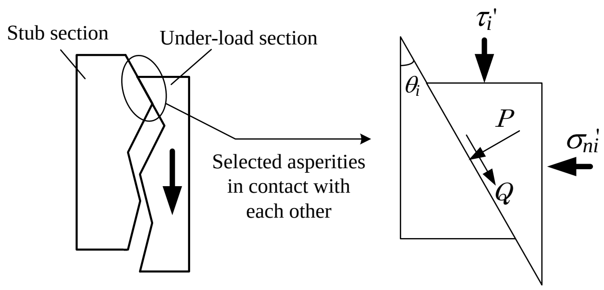

Figure 10 Asperities in contact with each other under stress

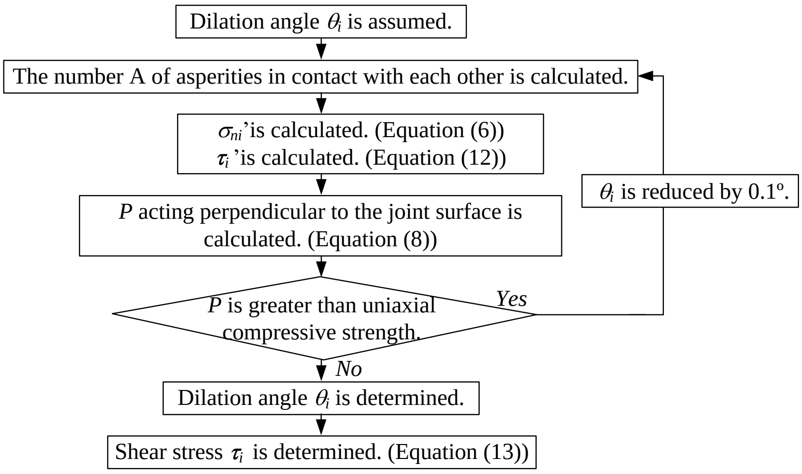

Figure 11 Flow chart in Step i

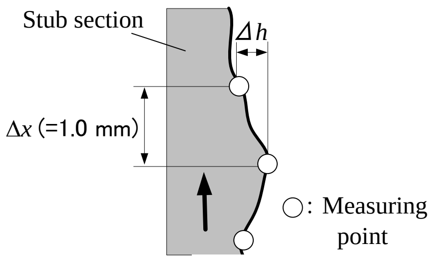

Slope angle of the asperity : $\theta = \tan^{-1}\Delta h/1.0$

Figure 12 Slope angle of an asperity

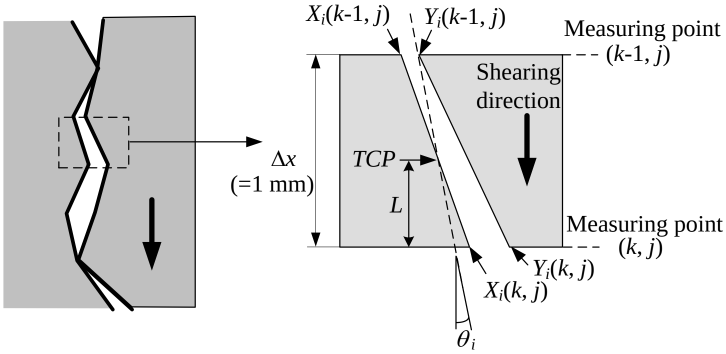

Figure 13 Concepts of *Weight* and *TCP*

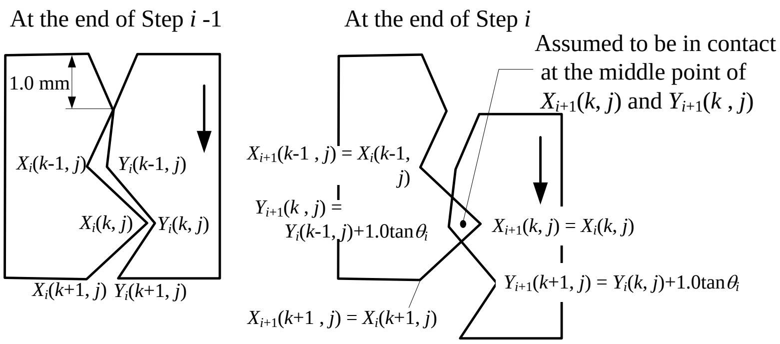

Figure 14 Coordinates at the end of Step *i*

Table 2 Analysis cases

No.	Crack width	Tapered angle of joint surface	Material strength (Uniaxial compressive strength)
1–9	0, 1, 2, 3, 4, 5, 6, 7, 8 mm	0°	36 N/mm^2
10–15	0 mm	5, 10, 15, 20, 25, 30°	36 N/mm^2

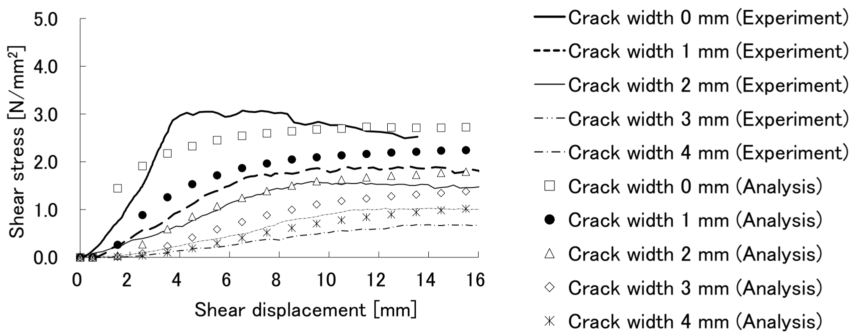

(a) Relationship between shear displacement and shear stress

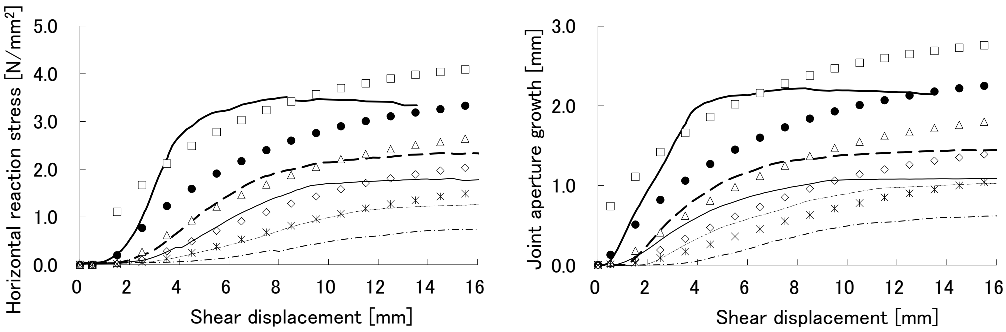

(b) Relationship between shear displacement and horizontal reaction stress

(c) Relationship between shear displacement and joint aperture growth

Figure 15 Results of analysis in comparison with those of experiment (crack width of 0 to 4 mm)

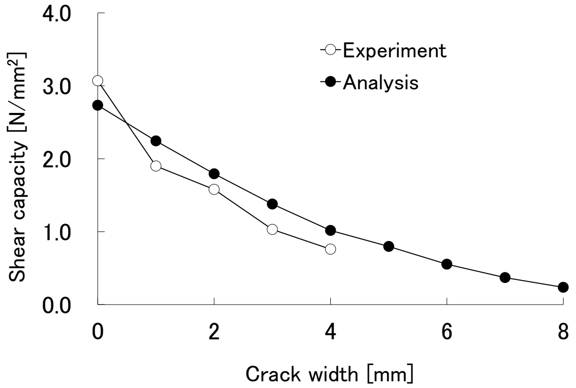

Figure 16 Relationship between joint aperture and shear capacity

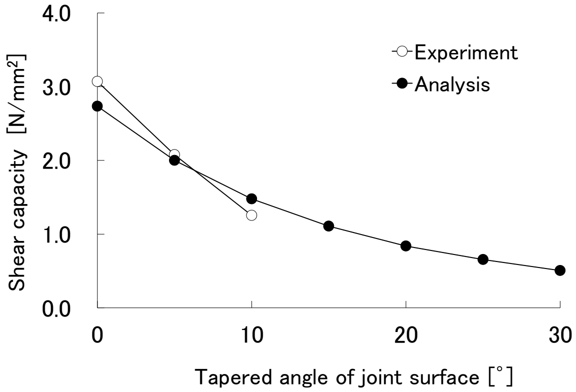

Figure 17 Relationship between tapered angle of joint surface and its shear capacity

(a) Sample A

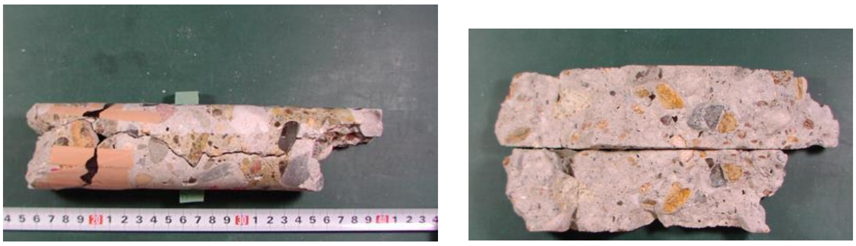

(b) Sample B

(c) Sample C

Figure 18 Core samples of joint surfaces

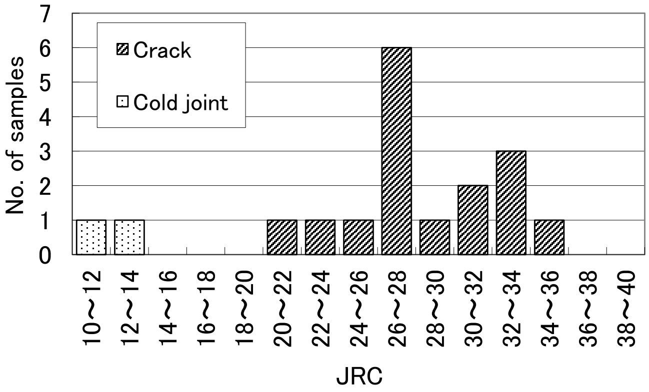

Figure 19 *JRC* values of joint surfaces on actual tunnels

Table 3 *JRC* values of joint surfaces made in beam shear test

Maximum aggregate size	*JRC* value
Without aggregate (mortar)	22
40 mm	36
20 mm	29

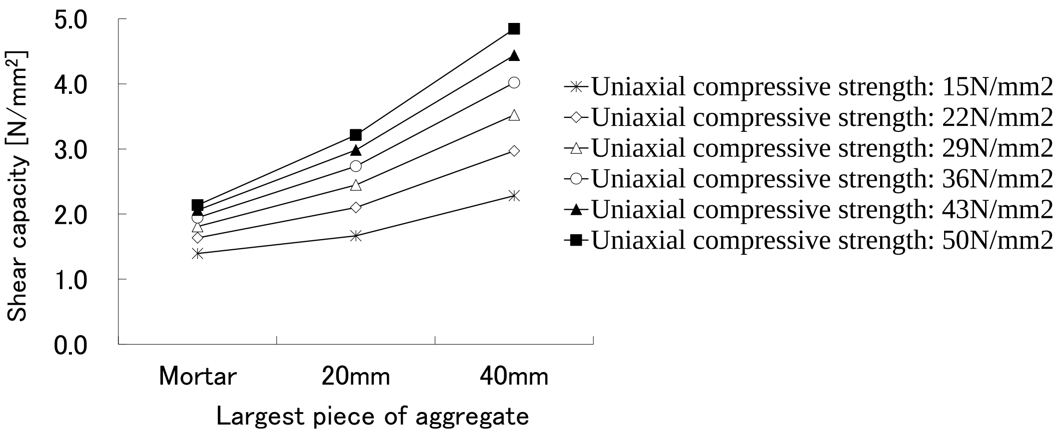

Figure 20 Calculated shear capacity (Tapered angle of joint surface: 0°)

Table 4 Uniaxial compressive strength of lining concrete (Miura et al., 1959)

Tunnel	Age*	No. of test pieces	Uniaxial compressive strength
No.3 Otoshibe (Tunnel arch)	14 years	6	25.8 N/mm^2
Obusu Tunnel (Side wall)	20 years	6	17.6 N/mm^2
(Arch)		6	18.1 N/mm^2
Shimokuno Tunnel (Side wall)	26 years	6	23.2 N/mm^2
(Arch)		6	14.7 N/mm^2
No.2 Yubiso Tunnel (Side wall)	29 years	2	16.8 N/mm^2

*: At the time of the investigation

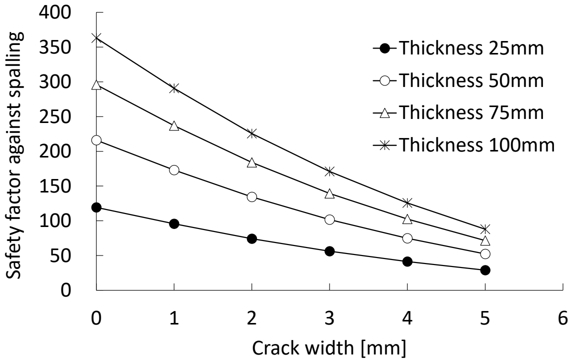

(a) *B* = 250 mm, *D* = 250 mm

Uniaxial compressive strength: 15 N/mm^2

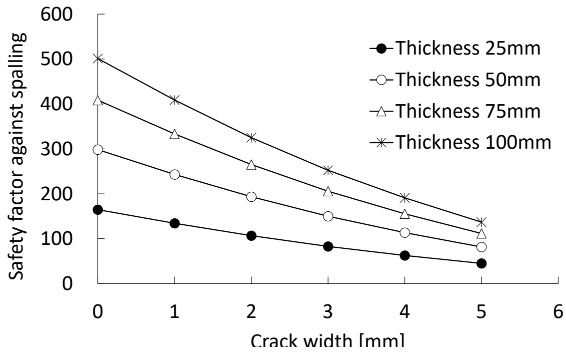

(b) *B* = 250 mm, *D* = 250 mm

Uniaxial compressive strength: 26 N/mm^2

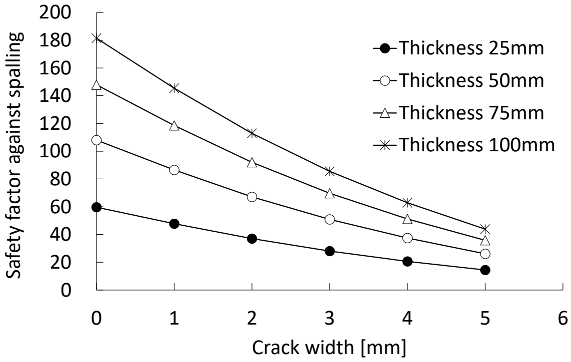

(c) *B* = 500 mm, *D* = 500 mm

Uniaxial compressive strength: 15 N/mm^2

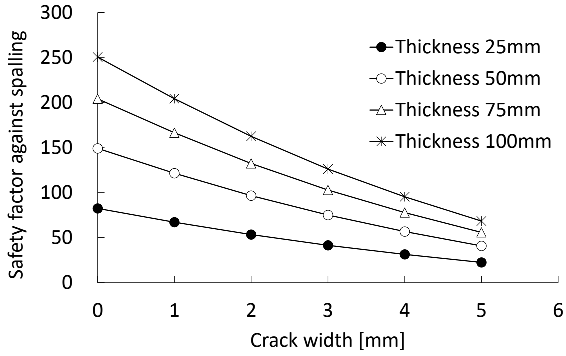

(d) *B* = 500 mm, *D* = 500 mm

Uniaxial compressive strength: 26 N/mm^2

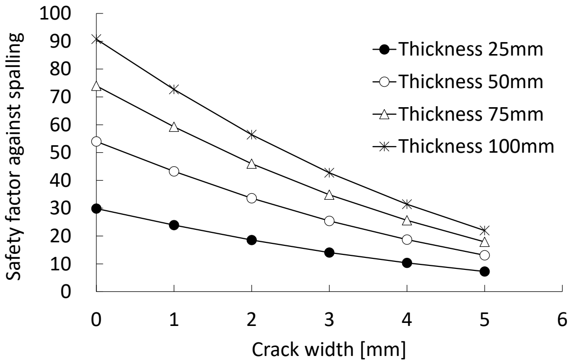

(e) *B* = 1000 mm, *D* = 1000 mm

Uniaxial compressive strength: 15 N/mm^2

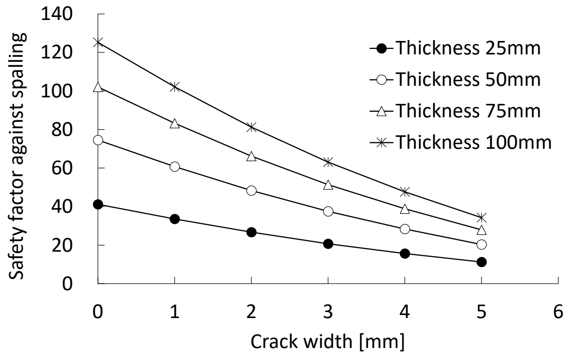

(f) *B* = 1000 mm, *D* = 100 mm

Uniaxial compressive strength: 26 N/mm^2

Figure 21 Calculated safety factor against spalling (Tapered angle of joint surfaces: 0°)

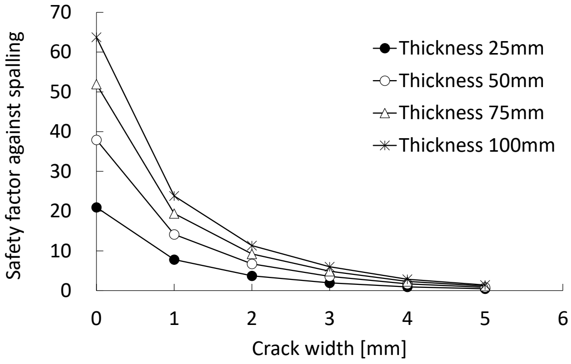

(a) B = 250 mm, D = 250 mm

Uniaxial compressive strength: 15 N/mm^2

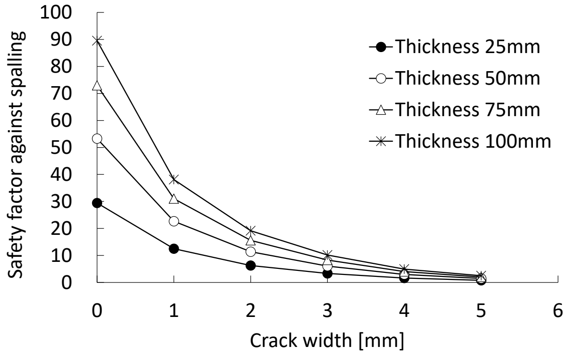

(b) B = 250 mm, D = 250 mm

Uniaxial compressive strength: 26 N/mm^2

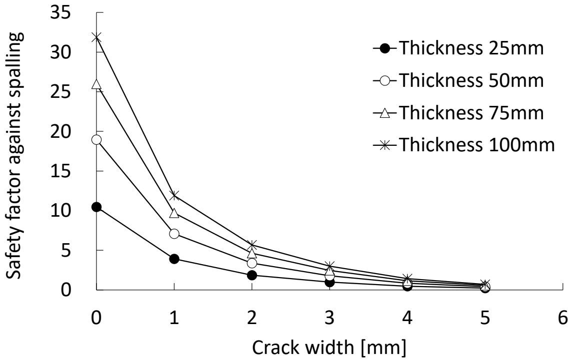

(c) B = 500 mm, D = 500 mm

Uniaxial compressive strength: 15 N/mm^2

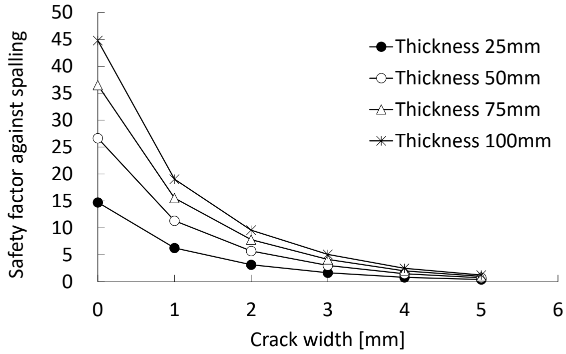

(d) B = 500 mm, D = 500 mm

Uniaxial compressive strength: 26 N/mm^2

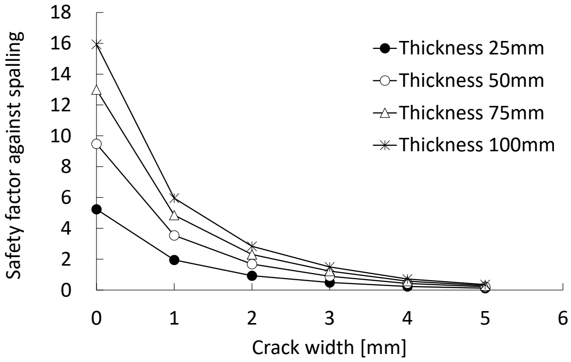

(e) B = 1000 mm, D = 1000 mm

Uniaxial compressive strength: 15 N/mm^2

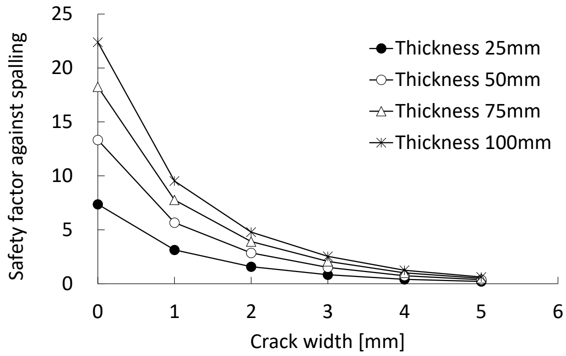

(f) B = 1000 mm, D = 100 mm

Uniaxial compressive strength: 26 N/mm^2

Figure 22 Calculated safety factor against spalling (Tapered angle of joint surfaces: 30°)

Table 5 Safety factor against spalling with taped angle of joint surface 30°

Size of chunk [mm]			Uniaxial compressive strength				
Width *B*	Depth *D*	Thickness *H*	15N/mm^2	22N/mm^2	26N/mm^2	29N/mm^2	36N/mm^2
250	250	25	1.98	2.78	3.34	3.69	4.50
		50	3.58	5.03	6.05	6.67	8.14
		75	4.90	6.89	8.29	9.14	11.14
		100	6.01	8.45	10.17	11.21	13.67
500	500	25	0.99	1.39	1.67	1.84	2.25
		50	1.79	2.51	3.03	3.34	4.07
		75	2.45	3.44	4.14	4.57	5.57
		100	3.00	4.22	5.08	5.61	6.84
1000	1000	25	0.49	0.69	0.84	0.92	1.12
		50	0.89	1.26	1.51	1.67	2.03
		75	1.22	1.72	2.07	2.28	2.79
		100	1.50	2.11	2.54	2.80	3.42